Near/Mid Infrared-Wavelength Study of the Interacting Galaxy Pair UGC 12914/5 -- "Taffy"

T.H. Jarrett, G. Helou, D. Van Buren, and E. Valjavec

Infrared Processing & Analysis Center

MS 100-22, Caltech

Pasadena, CA 91125

Emails: jarrett@ipac.caltech.edu; gxh@ipac.caltech.edu; dave@ipac.caltech.edu, eval@ipac.caltech.edu

J. Condon

National Radio Astronomy Observatory

520 Edgemont Rd, Charlottesville, Va 22903

Email: jcondon@nrao.edu

Received _____; Accepted _____

DRAFT rev 990328 ---

for submission to the Astronomical Journal

ABSTRACT

We report on an infrared 1 to 17 μm study of the nearby (cz = 4600 km/s) interacting spiral galaxy system, **UGC** 12914/12915 (VV 254), using the ground-based Palomar 200" telescope and PFIRCAM near-infrared detector and space-based mid-infrared imaging and spectral observations using ISOCAM and Phot-S on the Infrared Space Observatory (ISO). The system consists of two counter-rotating spirals having suffered a nearly face-on collision only ~10^7 years ago. In conjunction with radio observations we explore the complex gas/dust morphology of the post-collision disks, ring structures, current epoch of star formation, and the remnant connecting bridge: It is the unusual radio synchrotron bridge that this study was largely aimed at understanding.

Strong line emission from aromatic band features at 6.2, 7.7 and 11.3 μm are seen in both the mid-IR imaging and Phot-S spectro-photometry centered on the nuclei. The total mid-IR flux density is ~1.3 Jy, or about 5% of the total far-infrared flux density (IRAS bands). Our near/mid-IR data supports the hypothesis that the restricted form of galaxy-galaxy interaction—counter-rotating direct head-on collision between comparably massed spirals—has produced a large-scale dynamically expanding "ring" of recent star-formation and gas "bar" structure within the disk of UGC 12914. The nucleus and northwestern disk of UGC 12915 is undergoing vigorous star formation probably triggered by the interaction; consequently the burst must be ~10^7 years old. UGC 12914 appears to be more quiescent than its interloping twin, although there are signatures of massive star formation as revealed in the direct comparison between the radio, mid-infrared and Hα imaging. Within the connecting bridge region, the mid-infrared imaging reveals dust grains intermixed with the atomic hydrogen gas. The heating

mechanism for the hot dust is likely to be UV photons diffusing out from the galactic disks and the H II complex that is located along the extreme northeastern portion of the bridge: The grain emissivity, or mid-infrared intensity per atomic hydrogen column density ratio, is consistent with heating from the local (bridge) interstellar radiation field.

Subject headings: galaxies: individual (UGC 12914/12915, VV254) -- galaxies: interactions – Galaxies: ISM – Infrared: galaxies

1. Introduction

The nearby (60 Mpc for $H_0 = 75$ km/s/Mpc) interacting pair of galaxies, UGC 12914/5 (VV 254), possess a number of uniquely favorable characteristics for the study of spiral galaxy collisions, see Fig 1. Extensive study of the system in the radio (Condon et al. 1993) reveals that the galaxies are: (1) normal (pre-collision) spiral galaxies, (2) nearly parallel (<11 deg) in orientation of their respective disks, (3) in contra-rotation to each other, and (4) both moving roughly in the plane of the sky. The orbit and disk orientation facilitates clean separation on the sky of the disk and post-collision environment. Two newly formed large angular-size structures from the encounter are distinguished: the disk of UGC 12914 (southern most galaxy) appears to have a stellar ring roughly centered about the nucleus, and the system contains a very bright radio synchrotron "bridge" connecting the two spiral galaxies and earning the system its "Taffy" designation (see Fig 1). The collision has stripped H I gas from the respective disks leaving a gas material "splash" trail in the post-collision trajectory. Aligned linear polarization vectors show that magnetic fields anchored to the disk giant molecular clouds have been entangled and stretched out (like taffy candy) by the interaction. The strong magnetic fields lines, still attached

to their parent galaxies, trap cosmic ray electrons stripped during the encounter and act as a directional conduit for charged cosmic rays diffusing from the disks, resulting in a steep radio spectrum dominated by non-thermal synchrotron radiation. Additionally, the bridge is also remarkable in that it contains nearly one-quarter of the total hydrogen gas mass of the VV 254 system.

Not surprisingly the violent encounter has probably induced a burst of star formation in the disks, particularly UGC 12915, clearly evident in the optical and near-infrared data (Bushouse 1986; Bushouse & Werner 1990). The dynamical large-scale ring around UGC 12914 can be seen in both the optical and near-infrared (see Fig 1 - 3). The total far-infrared emission, a robust diagnostic of star formation, is strong enough to place VV254 in the IRAS bright galaxy catalog (Soifer et al 1989). The estimated star formation rate for the combined system is ~2-4 $M_{\odot}$/yr based on either the radio or the FIR data, which, as our ISOCAM data will show, is only a lower limit for the activity in the bright UGC 12915. What is not conspicuous at short wavelengths (including Hα line) data is the presence of the H I gas "bridge" (cf. Fig 2). Evidently the bridge does not contain a large population of stars, including massive stars, which would be easily traced via Hα emission given the lack of continuum emission from older stars. Due to the relative youth of the bridge (~10^7 years), an absence of a stellar population is not unexpected. It is also consistent with the small impact parameter "splash" class of bridge (Gerber et al. 1990; Appleton et al. 1996; Struck 1997) which are devoid of stars and may indicate that star formation on a large scale is inhibited by strong tidal forces.

Nevertheless, the bridge should contain, in addition to the atomic hydrogen, both molecular hydrogen gas and interstellar dust stripped from the parent galaxy(s), assuming the molecular gas/dust has not been destroyed by shocks from the interaction. Cold dust,

representing the bulk of the total dust mass, is traced by reprocessed short-wavelength photons emitted in the far-infrared, but unfortunately the VV254 system is not large enough in angular size to be fully resolved by IRAS (Fig 4). On the other hand, the presence of significant far-infrared emission in the bridge region is not consistent with the observed FIR to radio flux density ratio for the system as a whole. Condon et al (1993) point out that the total FIR emission observed for VV254, $\log(L_{ir}/L_{\odot;}) = 10.94$ is too low compared to the corresponding amount of total radio emission (due to the radio-loud bridge), whereas the ratio is "normal" (cf. Helou et al. 1999) if you exclude the bridge region from the calculation, which suggests that the bridge does not contribute to the far infrared. In order to understand the energetics of the bridge ISM, it is important that the actual dust column density be measured. IRAS does not have the angular resolution to properly measure the FIR emission between the galaxies, but ISO does have the required spatial resolution, sensitivity and spectral coverage in the mid-infrared (MIR) to measure emission presumably originating from small grains and molecules with fluctuating temperature well studied in the Milky Way. Even though this MIR dust emission traces only a small fraction of the total dust mass, ISO observations show that it is very closely correlated with the FIR dust emission in the quiescent and star-forming atomic and molecular gas (cf. Helou et al. 1999). ISO observations can not only reveal the presence of dust in the connecting bridge, but also allow comparison of the MIR energetics with the atomic hydrogen column density to help decode the effect of the recent galaxy-galaxy interaction on the material of the bridge and interstellar medium of the disks and nuclear regions. We report the results of new near- and mid-infrared observations made with groundbased telescopes and with ISOCAM using the LW1, LW2, LW8 and LW3 filters, covering 1 to 17 μm and PHOT-S spectro-photometry covering 3 to 11 μm in wavelength centered on the centers of the respective nuclei.

2. Data

The near-infrared J (1.3 μm), H(1.7 μm), & Ks (2.2 μm) imaging data were acquired with the Hale 200" telescope and Palomar prime-focus infrared camera (PFIRCAM; see Jarrett et. al. 1994) on Sept. 10 1998 under ideal photometric conditions. PFIRCAM employs a 256X256 HgCdTe array with 0.495" pixels, giving a total field of view ~2.1'X2.1'. The observations consisted of a nodding sequence between the galaxy field and adjacent blank sky fields. Positional dithering between sequence pairs minimizes the effects of masked pixels and flat-field variations, and provides a means to generate "sky" flat-field images used for pixel to pixel gain variation correction. The reduced images were registered and coadded to form deep exposure mosaics. The effective spatial resolution of the K_s data is ~1". UKIRT standards were used for calibration. The resulting surface brightness (1σ) sensitivity is ~21.3 mag per arcsec^2 at K_s-band and ~22.5 mag per arcsec^2 at J-band.

The ISOCAM data consists of four individual AOT (astronomical observation template) sets: 11 Jan 1997 (revolution 432), 25 Jun 1997 (rev 587), 25 Jun 1997 (rev 587), and 22 Jul 1997 (rev 614). The AOTs represent bundled data sets taken under different conditions, including spacecraft orientation, radiation field and pointing history (i.e., what ISOCAM was pointing at before observations of data set—an important initial condition factoring into successful transient removal; see below). Each set consisted of observations with LW1 (4.1 - 5.0 μm), LW2 (5.5 - 8.5 μm), LW8 (10.9 - 11.9 μm) and LW3 (12.2 - 17.0 μm), with 6" pixels at all wavelengths, and an effective resolution of about 7" to 9". A 3X3 raster map with 14" was used for each filter. The 14" spacing between dither positions turned out to be too small for construction of a reliable non-galaxy contaminated "sky" flat-field image (see below).

The data were reduced at IPAC using the standard reduction procedure and package CIA, including bad-pixel masking, (and masking of vignetted regions), dark/bias subtraction, deglitching (MMT routine; Starck et al. 1995), correction/removal of non-linear transient & pixel memory effects unique to ISOCAM data (cf. Cesarsky et al 1996 and Seibenmorgen et al. 1997), and flat-fielding. Due to the large angular size of VV254 compared to the pixel size and dither pattern, we were forced to use a standard "library flat" image (generated from ISOCAM observations obtained early in the mission) to perform flat-field division. The disadvantage of using this flat-field image is that vignetting effects are magnified and the corners of the resultant residual image are not truly flat. Consequently, the corners were masked from further reduction. Fortunately the central 70% or so of the resultant coadded image appears flattened to at least 5 - 10%. We checked for relative consistency between the different AOT observations by performing aperture photometry on each (four in total) of the fully reduced, corner-masked, sets of images, per filter. Since each AOT represents a different spacecraft orientation and transient environment, the four sets should reflect differences due to both the flat-field correction and artifacts introduced in deglitch and transient removal procedures. Apertures (radius=12") were centered on the nuclei of UGC 12914 and UGC 12915, the connecting bridge and on a blank region of sky. For the high snr measurements (nuclear regions), the relative rms scatter in the photometry is 5-10% for LW3, 4-8% for LW8, 3% for LW2, and 5-10% for LW1. For the low snr measurements (bridge and blank sky) the rms is consistent with being dominated by background noise and an additional 3-5% noise component, possibly due to variations in the zodiacal emission.

We conclude that the flat-field correction has introduced at most an additional 5% uncertainty in the relative flux between AOT observations. Since we have shown that the

individual data sets are consistent to within <10%, a co-addition of all images (per band) should improve the overall sensitivity by ~2. The resultant final "super" coadd is then used to compute flux densities and compare with other wavelength data. The remaining analysis refers to these final coadd images. The super-coadd has resampled 2" pixels and has been rotated to the standard 4-point cardinal sky orientation. The absolute calibration uncertainty is estimated to be <30%, which is the nominal ISOCAM absolute flux uncertainty. The images do show some residual non-linear background gradients (particularly LW1) which add (systematically) a few % to the overall uncertainty in the flux densities. The gradients are probably the result of the flat-field division in the longer wavelength images (in which the zodiacal background is strongest). The relatively poor quality of the LW1 data is largely unknown, but may be related to the short-wavelength detector itself.

PHT-S (PHT 40), a module of ISO-PHOT instrument (Lemke et al. 1996), is a linear 64-element (32 + 32) Si:Ga detector array covering two wavelength ranges: 2.5 - 4.9 μm with 0.04 μm resolution, and 5.9 to 11.7 μm with 0.1 μm resolution per element. Our PHT-S data consists of one individual AOT set: 11 Jan 1997 (rev 432). Two pointings were performed, one centered on UGC 12914 and the second on UGC 12915, with a 24" × 24" aperture. About 1300 seconds per pointing were accumulated using a 210" rectangular chopper throw pattern. The data were reduced at IPAC using the standard PHT interactive analysis (PIA) reduction package, and the latest (as of March 1999) calibration routines which correct for flux underestimation due to the finite chopping frequency. The relative (channel-channel) calibration is estimated to be good to 10 - 20%, and likewise the absolute calibration is probably good to 10 - 20. As a consistency check, in section 3.3.4 we will compare the spectroscopic flux of UGC 12915 with that measured with ISOCAM and LW2.

3. Results

3.1. Near-IR Images

The reduced NIR JHKs images are shown in Fig 2 with linear grey-scale and contour rendering. In addition, the lower-left panel is a map of the K_s-band (2.2 μm) continuum overlaid with atomic hydrogen column density contours to illustrate the large concentration of gas in the intergalactic medium and well beyond the outer low surface brightness NIR isophotes. Low surface brightness structures, including the tidal arms and large-scale ring, are more clearly seen with a composite J+H+K_s 3-color (RGB) image, Fig 3. Overlay contours of the radio continuum are in Fig 3b to visually delineate the thermal component (stellar photosphere radiation) from the non-thermal (cosmic ray synchrotron emission associated with massive star formation and supernovae).

The NIR is sensitive to light coming from the older stellar population and from red supergiants associated with massive star formation. Stellar light reveals the overall system morphology to be generally disturbed. The nuclei of UGC 12914/5 dominate the total near-IR emission, with prominent "red" dust lanes evident in the brightest nucleus, UGC 12915 (Fig 3) and an H II knot ~30" southwest of the nucleus (spatially correlated with Hα line emission). A tidal-warped spiral arm of UGC 12915 is seen to the northwest of the nucleus following the radio continuum (Fig 3). The disk of UGC 12914 is characterized by a bright nucleus, dust lanes extending 20-30" from the nucleus and bright "warp" features anchoring the north-south ends of the disk. A spiral arm extending above the northern "warp" feature appears to be tidally stretched by the interaction with UGC 12915. Moreover, a large-scale ring or branch of a spiral arm encircles UGC 12914, with the brightest section passing through the southwestern bridge

region (see Fig 3b). In spite of the ring presence, most of the connecting bridge region is devoid of near-infrared light. A summary of the global photometry for the system is given in table 1 and the corresponding colors (log of the integrated flux density ratio between J&K and H&K) in Table 2.

3.2. Mid-IR Images

The final coadd (average of four data sets) MIR images for the ISOCAM bands, LW1(4.5 μm), LW2 (6.75 μm), LW8(11.4 μm), & LW3 (15.0 μm), are shown in Fig 5. Radio continuum contours are included with the LW3 grey-scale image. The total 'effective' field of view is about 3 arcmin, with 2" pixels and an effective resolution of ~9". The nucleus of UGC 12915 is the brightest object in the field, approximately 50-60% brighter than the combined nucleus and adjacent knots (spatially coincident with the NIR "warp" knots; Fig 3 & 7) comprising the disk of UGC 12914; see table 1 for photometry, and table 2 for colors. The total integrated flux density of the system, UGC 12914/5 + Bridge is about ~1.3 Jy, which is about 20% of the total IRAS 60 μm flux density (6.3 Jy) and 10% of the 100 μm flux density (13.4 Jy).

The UGC 12914/5 nuclei supply the bulk of the MIR emission; nonetheless, the "bridge" is easily seen in LW2, LW8 and LW3 images. The bridge structure is more apparent when combining all three mid-IR bands into one color image (Fig 6). Here we paint LW2 = blue, LW8 = green and LW3 = red. The MIR bridge, presumably originating from Aromatic Features, the so-called Unidentified Infrared Bands, or UIB (Leger & Puget 1984; Desert et al. 1990; Schutte et al. 1998; Helou et al. 1999), commonly thought to be due to PAH (polycyclic aromatic hydrocarbons) molecules, or tiny carbonaceous grains. The MIR emission peaks at 6.2 μm & 11.4 μm are spatially coincident with the 1.49 GHz radio bridge (see overlay contours, Fig 6b)

and the H I line emission (contour overlay, Fig 2), corresponding to position ~00h01m39s, +23d29m30s (J2000). The integrated flux of the bridge is between 10 and 40 times fainter than the nucleus of UGC 12915. There is no detection of a stellar population in the bridge based on the LW1 image which should trace stellar photosphere emission from late-type stars and photo-ionization from hard UV photons via the hydrogen recombination line Brα at 4.1 μm. Warm dust emitting from the bridge region and abutting large-scale ring can be clearly seen in the LW2 and LW3 images (Fig 5 & 6). Quantitatively, the flux difference between LW1 and LW3 for the bridge is a factor of 3 smaller than that of the disk of UGC 12914, also consistent with a paucity of 4 μm emission in the bridge. As seen in the NIR, the ring or warped spiral arm passes through (in projection) the connecting bridge. This morphology is more clearly seen in (Fig 7) which overlays contours of NIR K-band on gray-scales of LW2 & LW3 images. The NIR light is presumably originating from an older population of stars, which would be consistent with the ring structure projecting against or belonging to a warped spiral arm.

3.3. Flux Density & Color Radial Profiles

Cross-section profiles are used to compare relative variations in the NIR to MIR bands, MIR broad-band spectrum, and in the IR to radio continuum ratio on small spatial scales. Three cuts are made, one passing through the disk of UGC 12914, one the disk of UGC 12915, and one orthogonal to the disks, passing through the connecting bridge and H II region southwest of UGC 12915 (see Fig 7). To increase the signal to noise (SNR), we integrate a small circular area (r = 6", equivalent to ~1.5 kpc) along the profile, with 2" steps between adjacent areas. We plot integrated flux density (in millijansky) and effective "colors", log of the flux density ratio between bands. Flux ratios are only computed for points in which the integrated flux density has an estimated SNR 5 in both bands being measured. Colors include: log[J/K], log[H/K],

log[LW2/LW3], [LW8/LW3] and log [radio/LW3].

3.3.1. Disk of UGC 12914

The radial profile and color plots are shown in Fig 8. The nucleus dominates the NIR surface brightness profile (with H-band in the lead), while the MIR is characterized by three nearly equally bright peaks separated ~20" (~6 kpc) from each other. The line cut results confirm the impressions one gets from the images, namely that the NIR morphology is very different from that of the MIR and radio. The NIR is tracing photospheric emission from the old (pre-collision) stellar population while the MIR is tracing small interstellar dust grains (Aromatic Feature dominated) which tends to highlight young massive stellar populations in the nucleus and possibly in the bright knots 6 kpc from the nucleus.

The NIR colors indicate a general reddening (in J vs. K) trend moving from the southern end of the disk to the northwestern end, with a prominent drop in the J and H flux density relative to K at the point where the northwestern "warp" feature is observed (see Fig). The reddening is probably selective extinction from dust in the ISM, but may also be from luminous bright stars (giants) in star formation regions. The MIR colors are mostly flat across the disk (to within the uncertainty in the ratio), while the radio to LW3 (15 μm) looks nothing like the infrared colors. The radio flux density is a factor of 5 to 10 times fainter than the MIR. There is a prominent rise in the radio continuum relative to LW3 along the northern side of the nucleus, with the color ratio peaking somewhere between the nucleus and the bright northern MIR knot (~3 to 5 kpc from the center). This radio "peak" may indicate non-thermal emission from cosmic rays diffusing outward from massive star formation regions (cf. Helou & Bicay 1993; Marsh & Helou 1998). The asymmetry between the northern and southern disk regions of UGC 12914

suggest that the ISM has been unequally affected by the recent passage of the interloping galaxy UGC 12915, which Condon et al. (1993) deduce to have passed through UGC 12914 just north of the nucleus.

3.3.2. Disk of UGC 12915

The disk/nucleus of UGC 12915 is remarkably different from that of its companion, UGC 12914. First, both the NIR and MIR reveal a singular broad and relatively smooth nucleus, Fig 9. The NIR colors show a reddening trend from the south toward the center of the nuclear region, but with the reddest colors occurring toward the northern side of the disk, ~12" (4 kpc) from the center. In contrast, there is a prominent "blue" rise in the J flux density near the northwest section of the tidal "hook" (20") probably associated with massive star formation (also revealed in Hα line emission). In the mid-infrared the colors exhibit even more dramatic behavior. The shortest bands, LW2 and LW8, significantly strengthen (relative to LW3) moving from the south, passing through the nucleus, and to the north, with colors reaching maximum 20" from the nucleus, again corresponding to the northwest tidal arm region (and roughly corresponding to the NIR color gradient). This behavior is most likely the result of strengthening in the PAH bands at 6.2 & 7.7 μm (convolved by LW2) and 11.4 μm (convolved by LW8), a compelling clue that a vigorous starburst is underway in the northern quadrant of the UGC 12915 disk. The radio continuum is consistent with this interpretation, exhibiting a steep rise in the flux density relative to LW3 passing from the southeast to the northwest, indicating that non-thermal radio emission (associated with massive star formation) is significantly higher in these regions.

3.3.3 Bridge Medium

The radial profile and color plots are shown in Fig 10. To summarize previous findings:

the connecting bridge between the interacting galaxies includes a bright HII region ~15" southwest of UGC 12915, prominent H I line emission & non-thermal synchrotron radiation and, to the south in projection, a large-scale ring of UGC 12914 (~30" northeast of UGC 12914), see Fig 3c. The HII region and ring are clearly seen in the NIR radial profiles with a sharp ("blue") rise in J/K and H/K toward the northern side of the HII complex. The J/K blue trend increases radially toward the ring, while H/K is mostly flat for the ring itself. Note however that the connecting bridge between the HII region and the ring is mostly devoid of any photospheric light at 1-2 μm (see also Table 1, Fig 2) so the flux ratios are susceptible to noise fluctuations and thus should be weighed accordingly. In the mid-infrared & radio the HII region complex is much more extensive with a broad shoulder extending ~25" from the nucleus well into the connecting bridge (Fig 10). The MIR indicates that dust grains must also belong to the connecting bridge (blending with the atomic and molecular gas components). The [LW8/LW3] color is mostly flat through the bridge, but with a sharp "red" depression south of the HII region toward the central bridge region (~30" from UGC 12915). The bridge colors then show a "blueward" trend moving southward into the ring area and toward the nucleus of UGC 12914. The color [LW2/LW3] also appears to be depressed between the HII complex and the ring, but again, the measurement sensitivity in this region is such that background noise is probably the dominant influence. Finally, the bridge colors show a "blueward" trend moving southward into the ring area and toward the nucleus of UGC 12914. The radio flux density actually dominates the total emission coming from the bridge (the only part of VV 254 where this happens). The radio continuum peaks in a region ~25" in length (corresponding to the "central" bridge) while the MIR broadly encompasses the northeastern HII complex and the southwestern ring of UGC 12914. The net result is that the radio to LW3 color is strongly peaked in the central bridge, somewhat anti-

correlated with MIR colors. The origin of the radio and mid-infrared emission in the bridge ISM is evidently from two unrelated sources, as we will argue in section 4.

3.3.4. Spectroscopy

The detailed composition of the MIR emission spectrum (shortward of 12 μm) coming from the nuclear regions is revealed with PHT-S spectroscopy (Fig 11). The Aromatic Features in emission are clearly seen at 6.2, 7.7 and 11.3 μm for the disk/nucleus of UGC 12915 (Fig 11a), dominating the total 6 to 12 λm band emission (corresponding to LW2, LW8 and partially, LW3). For comparison, a composite spectrum (Lu et al. 1998; Helou et al. 1999) comprised of many quiescent (normal) spiral galaxies is overlaid in black (solid continuous line) to illustrate the aromatic emission features and underlying continuum shortward of 6 μm. The presence of these line emission features is strongly correlated with heating by stars (via star formation and also from older populations) in normal galaxies and in infrared-luminous starburst galaxies (but is generally not found near AGNs since hard UV radiation destroys the small grains and UIB carriers; cf. Boulanger 1998; Boselli et al. 1998).

Comparing the ISOPHOT and ISOCAM measurements for UGC 12915, the integrated flux density between 5 and 8.4 μm is 210 mJy, dominated by the 6.2 and 7.7 μm emission lines, and the LW2 flux density (computed in a similarly sized area centered on the nucleus of UGC 12915) is 183 mJy, or a difference of about 15%, within the measurement uncertainty. At the short end, the 2.5 to 4.5 μm spectrum is dominated by noise, while no Brσ recombination (at 4.1 μm) or PAH emission line at 3.3 μm is discernable.

Finally, UGC 12914 is considerably fainter than its companion and consequently its spectrum (Fig 11b) is mostly subjugated by background noise. Only the 6.2 and 7.7 μm lines are

clearly discerned from the noise and underlying continuum. The 7.7 μm line, with an integrated flux density of ~50 mJy +- 30%, is strangely blue-shifted with respect to the 6.2 μm line and the composite spectrum. Given the low SNR and the inconsistent line positions, the spectrum for UGC 12914 should be used with caution.

4. Discussion

Infrared imaging reveals that the UGC 12914/5 system can be decomposed into three principal morphological components (size ~10 kpc): two multi-peaked "disks" or "main disks," (dominating the total MIR flux), large-scale ring or tidal arm of UGC 12914, and connecting bridge. The energetics and general ISM environment are vastly different, with disks subject to a vigorous starburst (UGC 12915) or normal star formation phase (UGC 12914), the ring/arms modified by an expanding shock wave from the collision (but nonetheless, very little star formation), and the connecting bridge constrained by strong magnetic fields trapping electrons stripped in the encounter and channeling energetic cosmic rays from massive star formation regions. Given the relatively brief evolution from the initial encounter to the present state of the system, these regions are likely to evolve dramatically in the next ~10^7 -10^8 years.

4.1 The Disk/Nucleus of UGC 12914/5

For the VV254 system, the surface brightness averaged on scales of ~3 kpc varies widely among emission bands, from optical (0.6 μm and Hα at 0.66 μm), NIR (1-2 μm), MIR (3 - 17 μm) and radio (20 cm), and moreover the two galaxies appear quite different as viewed in the MIR and radio. The short wavelength emission is significantly attenuated by dust

extinction—rendering, for example, Hα to UV radiation comparisons suspect—in the core and disk of UGC 12915 and to a lesser extent in the disk of UGC 12914. In the MIR and radio, the nuclear region of UGC 12915 exhibits a strong peak at the position of the putative nucleus and a broad shoulder extending to the north into the tidal "hook" structure, also roughly corresponding to Hα emission peaks (Bushouse & Werner, 1990). Numerical simulations of galaxy-galaxy interactions show that star formation is enhanced in the post-collision disks due to molecular cloud collisions (cf. Olson & Kwan 1990) which is consistent with the observed Hα /MIR/radio spectrum of UGC 12915 and the total FIR flux of the system. Furthermore, the correlated radio-MIR morphology in UGC 12915 (Fig 9) is pretty typical of star forming disks, where massive star formation produces both the UV radiation field that transiently heats dust grains to emit in the MIR and the energetic cosmic rays (via supernovae) to engender synchrotron radiation (cf. Helou et al. 1985, and Condon 1992 review). In the southern galaxy, UGC 12914, MIR emission delineates three equally bright peaks, including the nucleus, spanning the optical/NIR disk (~18 kpc) of UGC 12914, but with a total MIR and radio flux nearly a factor of two less than its northern companion. The radio is enhanced relative to the MIR along the northeast side of the disk (third peak), corresponding to the junction between the disk and tidal arm and ring structure of UGC 12914. The MIR emission peaks roughly correspond to enhanced Hα emission, one bright HII complex to the southeast and a string of HII regions extending to the northwest along the disk and warp feature (cf. Bushouse & Werner 1990). The MIR peaks, therefore, represent "hot spot" regions undergoing massive star formation probably induced or enhanced from the interaction. Collision-triggered starbursts are a common feature of interacting galaxies, and are a prime candidate for the engines that power ultra-luminous infrared galaxies (cf. Genzel, Lutz & Tacconi, 1998; Genzel et al. 1998). In the NIR, the peaks appear more linear

and resemble an extended (several kpc) bar structure not unlike NGC 7552, a known barred spiral (also see Mazzarella et al. 1994 for similar NIR barlike morphology in NGC 7469). In any case, the overall level of star formation in UGC 12914 appears to be half of that in its northern based on the radio and MIR fluxes between the two galaxies. The pre-collision molecular gas mass differences and encounter geometry can account for the post-interaction star formation activity. UGC 12915 is observed to have a higher H_2 mass fraction as deduced from molecular CO data (Min Yun, private communication), and UGC 12915 is more compact than its companion (as measured from the stellar light); thus the density of molecular clouds and material near the nucleus is more susceptible to shock induced star formation from the encounter.

The PHOT-S 3-12 μm spectrum concurs with the scenario above. The MIR emission from the nuclear regions of UGC 12915 is dominated by Aromatic Features in emission, characteristic of star formation rather than a hard-UV producing (Genzel et al. 1998; Puget & Leger, 1989). Based on the estimated time-scale of the interaction ~few$X10^7$ yrs, deduced from the spectral-steepening of the radio spectrum index of the "post-interaction" zone compared to that of the disks , and the relative mass and velocity differential between the spirals (Condon et al. 1993), the UGC 12915 starburst is early in its life-cycle.

4.2 The Ring of UGC 12914

The formation of expanding rings (Lynds & Toomre 1976; Theys & Spiegel 1977; Appleton & James 1990; see also review from Barnes, 1992) in the VV 254 encounter is possible given the conditions that it satisfies, including a near head-on collision (impact parameter $r_{min} < r_{disk}$) between comparably massed spirals and counter-rotating disks. Condon et al (1993) deduce from their radio velocity maps of VV 254 that UGC 12915 penetrated the disk of UGC 12914

just north of its nucleus, so that a ring may have formed in the larger UGC 12914. A slight off-center encounter will result in an "open" ring , offset from nucleus. Both optical and NIR emission (Fig 1 - 3) reveal an elliptical ring-like feature enveloping UGC 12914. The large scale ring extends some 1.8' (30 kpc) across, with the brightest arcs of the ring located within the connecting bridge field. There is some hint of massive star formation in the ring from the Hα line emission (Bushouse & Werner 1990). The MIR emission clearly outlines the rings in the bridge area and the northeast of UGC 12914 coincident with a string of HII regions defining the northern section of the ring, but the ring is not obvious elsewhere (Fig 6). The MIR (5 to 17 μm) ring emission is not spatially correlated with the radio continuum. The H I line map (Fig 2) does not clearly trace the ring, even though the H I gas extends well beyond the radio continuum and the faint optical light contours, but it is interesting to note that the extreme west-northwestern edge of the H I column density map corresponds to the NW ring arc. In summary, the ringlike structure appears to consist of stars, presumably from an old disk population of the pre-collision disk, and a few isolated pockets of massive star formation, with little or no evidence of enhanced atomic gas column density or a systemic starburst associated with the expanding shock wave. It may be that massive stars will form in the future (delayed onset of star formation triggered by the expanding shock) or that the molecular gas density is insufficient to fuel star formation (cf. inner ring of the Cartwheel galaxy, Higdon 1996). Though less likely, it is also possible that the ring is in fact a tidal arm of UGC 12914. N-body simulations of the VV 254 system are needed to help decode the nature of the ring and spiral-arm structure.

4.3. The Bridge

The connecting bridge region of VV 254 is remarkable in that it contains a *significant* atomic gas column density (~10^{21} cm^{-2}), accounting for nearly one-quarter of the total H I mass

of the system (Fig 2). Only a few nearby systems show significant gas fractions outside of their post-collision disks, including NGC 4814/20 (van de Hulst & Hummel 1985) and NGC 7714/5 (Smith et al. 1997). Moreover, the bridge is unique in that it is most conspicuous in the radio, dominated by synchrotron and inverse-compton radiation from cosmic ray electrons trapped in the post-collision magnetic field stretching between the disks. The optical and NIR clearly delineate the H II region complex southwest of UGC 12915 (see also Hα images in Bushouse and Werner 1990) and the ring projected against the southern half of the bridge, but do not show otherwise any evidence of a stellar population in the bridge (Fig 1 - 3). Consistent with a "splash" bridge formation scenario (cf. Struck 1977), the MIR emission indicates significant dust content in the bridge, including the gap between the H II region and the ring (Fig 6). The origin of the MIR emission is probably dust grains re-radiating in the 5 - 25 μm window. Since we do not have a spectrum of the bridge MIR emission, it is not possible to cleanly separate line emission from the underlying continuum. There are two possible heating mechanisms for the dust detected in the broad band ISOCAM data: UV radiation from the galaxy disks, and collisional heating from the relativistic electrons in the bridge.

Consider first electron to dust grain collisions. Given the steep radio spectrum of the bridge, the cosmic ray heating mechanism is likely to be negligible for the following reason. Cosmic ray electrons both ionize the atomic hydrogen and free-free scatter off of ions, but the power lost per electron by ionization is independent of electron energy, so the fractional losses are greatest for low-energy electrons (Pacholczyk 1970; Condon 1992). The signature for low-energy electrons is a flat radio spectrum since ionization losses reduce the spectral index, while free-free losses do not affect the spectrum. On the other hand, synchrotron and inverse-Compton losses are both proportional to energy squared, so they steepen the radio spectrum. Hence, the

observed steep radio spectrum suggests that the dominant energy-loss mechanism is probably synchrotron radiation or inverse-Compton radiation, so low-energy electrons only minimally contribute toward heating the ISM. Electrons may still be heating the dust grains, but they are unlikely to be the main component.

Thus, we are left with an ambient UV radiation field as the likely heating source of the dust and ISM. To explore the radiative heating hypothesis, we need to address two key issues: (1) is there enough dust to account for the MIR emission and (2) is the local radiation field strong enough to power the dust emission? Our understanding of the relationship between radiation fields, gas and dust has been greatly advanced over the last decade thanks to IRAS. For example, the gas to dust correlation is well established for FIR emission originating from Milky Way cirrus clouds and from the local solar neighborhood (Boulanger & Perault 1988; Boulanger et al. 1996). Additionally, the FIR to atomic gas column density relation persists in nearby galaxies, particularly for the diffuse (optically thin) components, although for the more complicated components (dense molecular clouds and H II regions) the yield is more uncertain (cf. Walterbos & Greenwalt 1996). Finally, the gas to dust correlation appears to extend to shorter wavelengths, <12 μm, including regions in which Aromatic Feature emission dominates the MIR spectrum (cf. Desert et al 1990; Jenniskens & Desert 1993); thus we may conclude, the warm dust (T > 100 K) is sufficiently mixed with the more prevalent cold dust (T < 20K) in the Solar neighborhood and in normal galaxies. The gas to dust emissivity diagnostic can be used to discern the nature of the MIR emission in VV254. The bridge is far enough from the bright nuclear disk(s) and H II regions that the radiation environment of the bridge is analogous to that of cirrus clouds above the disk of the Milky Way. If the intensity of the radiation field in the bridge is similar to that of the galactic cirrus (both in total intensity and in the UV photon

spectrum), then the MIR (and FIR) should similarly scale with the atomic gas column density. The bridge interstellar radiation field is probably composed of mostly non-ionizing photons originating from the disks and, to a lesser extent, OB star producing UV photons diffusing outward from H II regions (including or dominated by the complex to the southwest of UGC 12915). The detailed nature of the interstellar radiation field in spiral galaxies is, however, still a much debated and open topic (cf. Devereux & Young 1990; Xu & Helou 1995; Walterbos & Greenwalt 1996; Devereux et al. 1997). The following analysis does not assume what photons are actually heating the diffuse bridge dust, but instead assumes that the heating source (radiation field) is similar to what is observed in the solar neighborhood and upper cirrus clouds.

We begin with the gas content of the bridge. The atomic hydrogen column density (see Fig 2 overlay), measured by Condon et al (1993), is ~3×10^{21} cm^{-2} in a 18" FWHM centered on the bridge. The bridge MIR integrated flux densities (20" diameter aperture) are given in Table 1. Using the flux convention and formalism of Boulanger & Perault 1988, we convert the flux densities to intensity: $4\pi\nu I_\nu$ (MJy per steradian), normalize to the gas column density and compute the dust emissivity, or the MIR intensity per hydrogen atom. The emissivity reflects the expected MIR or FIR emission given an observed hydrogen column density, assuming that the 21-cm radio emission (from which the column density is derived) is optically thin and dust emission associated with molecular gas in the bridge is relatively minor. If the bridge radiation field intensity is similar to that of the local Solar neighborhood and in high Galactic latitude cirrus clouds (relatively low gas density molecular clouds with little if any star formation), then the gas column density-normalized emissivity should be the same as that seen in the Milky Way. The VV254 dust to gas emission spectrum results are given in Table 3. It is instructive to compare our MIR measurements with IRAS 12-μm solar neighborhood values (as given in table

2 of Boulanger & Perault 1988, corresponding to the emission spectrum of high-galactic latitude cirrus clouds). For LW8 (11.4 μm) and LW3 (15 μm), largely overlapping with the IRAS 12 μm band, the combined dust emission per H atom agrees within a factor of 2 with that seen in Galactic cirrus clouds. This result suggests that the bridge radiation field intensity is similar to that of the Solar neighborhood. Given the location of the bridge with respect to the disks and nearest H II complexes, ~6 to 7.5 kpc, the system geometry and the comparable stellar populations (of late-type spiral galaxies), the bridge UV radiation field is analogous to that expected for Galactic cirrus hovering above the disk of the Milky Way. If we assume that the bridge radiation field is comparable to the Solar neighborhood value (or at least to within ~2 in intensity), then the observed MIR (LW3) emission is consistent with the expected column of dust based on the observed H I column density.

In order to understand better the emission mechanism of the MIR radiation, in particular disentangling the continuum from line emission at wavelengths shortward of 12 μm, we consider the detailed work of Desert et al (1990). Using IRAS and ground-based NIR and sub-mm observations of the solar neighborhood and galactic cirrus, Desert et al (1990) modeled the expected dust emission spectrum subject to a varying range in the total intensity levels of the interstellar radiation field (ISRF). For the NIR and MIR bands, they used a two component dust model: very small grains (continuum) and PAHs (line emission). The grain/PAHs are transiently heated from single photon absorption coming from the ISRF, whose intensity is varied over a large range (orders of magnitude). Employing the flux unit convention of Desert et al (1990), Table 3 lists the VV 254 emissivity values, I_ν/N_H, which can be directly compared to the emission spectrum of the Desert et al (1990) model from their figure 4 and table 3. At the longest wavelengths, LW3, which is mostly free of line emission, agrees quite well, ~10%, with

predicted continuum emission from very small grains. At 11 μm, LW8 includes a very strong Aromatic feature (see Fig 11) accounting for the largest emissivity value, 1.2×10^{31} W/H atom, which is a factor of ~2 to 3 smaller than the Galactic cirrus value. Between 5 and 9 μm, spanning LW2, in which the MIR is dominated by two Aromatic Features (Fig 11), the VV254 dust emissivity agrees to within ~2 (again it is smaller) with the Galactic cirrus value. These differences are probably not all that significant given the strengths of the emission lines and probable differences (if slight) in the interstellar radiation fields. Finally, at the shortest wavelengths, LW1 (4-5 μm), subject to continuum emission only, the VV254 upper limit emissivity value is a factor of ~3 higher than the model-predicted value, comparable to within the measurement uncertainty. We may conclude that the intensity of dust emission coming from the VV 254 bridge region is consistent with the observed atomic gas column density. We caution however, that since molecular gas (traced via CO line emission) is observed in the bridge, the atomic gas column density must therefore underestimate the total gas column density in the bridge and some fraction of the MIR emission must be associated with the H_2 gas. Hence, the MIR to N_H ratio is likely to be an upper limit (cf. Desert et al 1990; Walterbos & Greenwalt 1996; Boulanger et al. 1996). Sensitive isotopic CO observations are needed to measure the total H_2 mass fraction in the bridge region in order to estimate the contribution of MIR emission from molecular gas.

5. Summary

For the interacting galaxy system UGC 12914/5 (VV 254) we have acquired new deep ground-based near-infrared imaging and spaceborne mid-infrared imaging and spectroscopic data using the Infrared Space Observatory. Our ISOCAM imaging data cover wavelengths

between 4 and 17 μm spatially resolving the system, composed of two morphologically disturbed spiral galaxies, large scale dynamical ring and a connecting intergalactic bridge. The total mid-IR emission is dominated by the nucleus of the more compact companion, UGC 12915 (northern galaxy), having nearly double the mid-IR photons as compared to the ringed UGC 12914 (southern galaxy). The total mid-IR flux density is ~1.3 Jy, or about 5% of the total far-infrared flux density (IRAS bands). The near/mid-infrared in conjunction with radio continuum data indicate that UGC 12915 is now undergoing vigorous star formation in or near its nucleus while UGC 12914 is more quiescent (at least in its current state), and thus the off-center collision has influenced the ISM evolution unequally in the two galaxies. A large-scale ring, resonantly induced by the nearly face-on collision, is detected in LW2 (6 μm) and LW8 (11 μm) bands.

Optical and near-infrared imaging data do not reveal the central gas bridge, although they do reveal a giant H II region seen in Hα just south of UGC 12915 in what appears to be the extreme northern extension of the bridge. In the far-infrared, IRAS does not have the spatial resolution to separate the two galactic nuclei or clearly resolve the bridge. Warm/hot dust in the nuclei and bridge is, however, resolved and detected with our ISOCAM data using the LW1, LW2, LW8 and LW3 filters, covering 4 to 17 μm in wavelength. VV254 is thus one of the few interacting systems in which significant dust emission is seen well outside of the disks of progenitor galaxies. Thermal continuum radiation from very small dust grains and strong line emission from aromatic band features at 6.2, 7.7 and 11.3 μm are seen in both the mid-IR imaging and Phot-S spectro-photometry centered on the nuclei and their connecting bridge. The mid-infrared morphology of the disk/nuclei regions resemble that of the 1.49 GHz radio continuum but not of the intergalactic bridge, suggesting that the origin of the radio continuum (non-thermal synchrotron) and mid-infrared emission (thermal heated dust) are unrelated in the

bridge. The source of the mid-infrared radiation in the connecting bridge is likely due to transiently heated dust—the product of energetic photons diffusing out from the disks. The dust emissivity is in correct proportion to the observed atomic gas column density, assuming the radiation field transiently heating the small dust grains is similar in intensity to what is observed in the solar neighborhood and high galactic latitude cirrus clouds. The detailed nature of colder dust ($T < 100K$) is still uncertain owing to lack of resolution in the FIR; fortunately the required observations will be possible with the next generation of IR space telescopes (e.g., SIRTF) and ground-based sub-mm arrays.

We would like to thank the ISO staff at IPAC for their help, particularly, Ken Ganga and Nanyao Lu. We thank Joe Mazzerella for useful discussions and Jim Cordes (Cornell U) for help with obtaining the Palomar data. This work would not have been possible without the help of M. Kessler who rescheduled our ISO observations to accommodate visibility restrictions. This work was supported in part by the Jet Propulsion Laboratory, California Institute of Technology, under a contract with NASA. We also acknowledge support from NASA ISO data analysis funding, courtesy of M. Bicay.

6. References

Appleton, P.N., Charmandaris, V. & Struck, C. 1996, ApJ, 468, 532.

Appleton, P.N., & James, R.A. 1990, in Dynamics & Interactions of Galaxies, ed. R.Wielen, p. 200.

Barnes,J, & Hernquist, L. 1992, ARAA, 30, 705.

Boselli,A., Lequeux,J., Sauvage,M., Boulade,O., Boulanger, F. 1998, A&A, 335, 53.

Boulanger, F. 1998, IAU-SYMP (179), p 153.

Boulanger, F., Abergel, A., Bernard, J.P., Burton, W.B., Desert, F.X., Hartmann, D., Lagache, G. & Puget, J.L. 1996, A & A, 312, 256.

Boulanger, F., & Perault, M. 1988, ApJ, 964.

Bushouse, H.A. 1987, ApJ, 320, 49.

Bushouse, H.A. & Werner, M.W. 1990, ApJ, 359, 72.

Cesarsky, d. et al. 1996, A&AL, 315, L32.

Condon, J.J. 1992,, ARAA, 30, 575.

Condon, J.J., Helou, G., Sanders, D.B., Soifer, B.T. 1993, AJ, 105, 1730.

Desert, F.X., Boulanger, F., & Puget, J.L. 1990, 237, 215.

Devereux, N.A. & Young, J. 1991, 103, 1536.

Devereux, N.A., Duric, N. & Scowen, P.A. 1997, AJ, 113, 236.

Genzel, R., Lutz, D., Sturm, E., Egami, E., Kunze, D., Moorwood, A., Rigopoulou, D., Spoon, H., Sternberg, A., Tacconi-Garman, L., Tacooni, L., & Thatte, N. 1998, ApJ, 498, 579,

Genzel, R., Lutz, D., & Tacooni, L., 1998, Nature, 395, 859.

Gerber, R., Lamb, S., Miller,R., & Smith,B.F. 1990, Dynamics and Interactions of Galaxies, ed. R. Weilen (Springer Berlin), p. 223.

Helou, G., Soifer, B.T., & Rowan-Robinson, M. 1985, 298, L7.

Helou, G., Lu, N.Y., Werner, M.W., Malhotra, S. & Silberman, N. 1999, ApJL, in press.

Jarrett, T.H., Beichman, CA., Van Buren, D., Gautier, N., Jorquera, Bruce, C. 1994, in Infrared Astronomy with Arrays, ed. I.S. McLean, Kluwer, p. 293.

Jenniskens, P. & Desert, F.X. 1993, A&A, 275, 549.

Leger, A. & Puget, J.L. 1984, A&A, 137, L5.

Lemke, D. et al. 1996, A&AL,315,L64.

Lu, N.Y., et al. 1999, in preparation.

Mazzarella, J.M., Voit, G., Soifer, B.T., Matthews, K, Graham, J.R., Armus, L. & Shupe, D. 1994, AJ, 107, 1274.

Olson, K. & Kwea, J. ApJ, 349, 480.

Packolczyk, A.G.. 1970, Radio Astrophysics. (Freeman, San Franscisco).

Puget, J.L., & Leger, A. 1989, ARA&A, 27, 161.

Siebenmorgan, R., Starck, J., Cesarsky, D., Guest, S., & Savage, M. 1997, ISOCAM Data User's manual, Ver. 3.0.

Schutte, W.A. et al. 1998, A&a, 337, 261.

Sellgren, K. 1984, ApJ, 277, 623.

Smith, B.J., Struck, C. & Pogge, R.W. 1997, ApJ, 483, 754.

Soifer, B.T., Boehmer, l., Neugebauer, G., & Sander, D.B. 1989, AJ, 766.

Starck, J., Bijaoui, A. & Murtagh, F. 1995, "Multiresolution Support Applied to Image Filtering and Deconvolution", in CVIP: Graphical Models & Image Processing, V. 57, 420.

Theys, J.C., & Spiegel, E.A. 1976, ApJ, 208, 650.

van der Hulst, J. & Hummel, E. 1985, A&A, 150, L7.

Walterbos, R.A. & Greenawalt, B. 1996, ApJ, 460, 696.

Xu, C. & Helou, G. 1995, ApJ, 446, 909.

Figure Captions

Fig 1—VV254 as seen in the optical and radio wavelengths. The gray-scales correspond to the Digital Sky Survey (DSS) image overlaid with radio continuum contours. The 1.49 GHz total-intensity contours are from Condon et. al. (1993). The contours range from 0.1 to 7 mJy/beam (5" FWHM), with successive contours scaled by sqrt(2).

Fig 2—VV254 as seen in the near-infrared. Clockwise: panels are gray-scale/contour overlays of J band (1.3 μm) , H band (1.6 μm) , & K_s band (2.2μm). Lower left panel shows the K_s image overlaid with contours of atomic hydrogen column density, N_H (from Condon et. al. 1993). Density contours range from 3.4×10^{20} to 2.7×10^{21} cm^{-2}.

Fig 3—Near-infrared 3-band composite image of the VV 254 system. The J, H & K_s bands are RGB color-combined as follows: J (1.3 μm) == blue, H (1.6 μm) == green, & K_s (2.2μm) == red . (a) contrast to show high surface brightness features, (b) contrast to show low surface brightness emission. The contour overlay corresponds to 1.49 GHz radio continuum emission. Contours range 0.1 to 7 mJy/beam (5" FWHM), with successive contours multiplied by sqrt(2).

Fig 4—VV254 as seen in the far-infrared. Clockwise: panels are gray-scale/contour overlays of IRAS 12, 25, 60 & 100 μm coadd images, resolution enhanced with IPAC deconvolution algorithms. The integrated flux densities for the combined UGC 12914/5 system are 0.43, 0.88, 6.3 & 13.4 Jy at 12, 25, 60 & 100 μm, respectively.

Fig 5—VV254 as seen in the mid-infrared. Clockwise: panels are gray-scale/contour overlays of ISOCAM LW1 (4.1 - 5.0 μm), LW2 (5.5 - 8.5 μm), LW8 (10.9 - 11.9 μm), and LW3 (12.2 - 17.0 μm). The lower left panel (LW 3 image) includes contours of the 1.49 GHz radio

continuum, ranging from 0.1 to 7 mJy/beam (5" FWHM).

Fig 6—Mid-infrared 3-band composite image of the VV 254 system. The LW2, LW8 & LW3 bands are RGB color-combined as follows: LW2 (6.8 μm) == blue, LW8 (11.4 μm) == green, & LW3 (15 μm) == red. (a) contrast to show high surface brightness features, (b) contrast to show low surface brightness emission. The contour overlay corresponds to the 1.49 GHz radio continuum emission. Contours range 0.1 to 7 mJy/beam (5" FWHM), with successive contours multiplied by sqrt(2).

Fig 7—Near-infrared and mid-infrared emission from VV 254. Panels are log-stretched gray-scale images of LW2 (5.5 - 8.5 μm) and LW3 (12.2 - 17.0 μm) overlaid with K band (2.2 μm) contours, ranging from 0.01 to 0.35 mJy/arcsec. Cross-section slice cuts (see Fig 8) through the disks of UGC 12914/5 and the connecting bridge region are denoted with thick solid lines.

Fig 8—Cross-section flux density & color profile of the UGC 12914 disk. At each point along the cross-section (see Fig 7) the flux density is integrated in a 6″ radius circular aperture. (a) near-infrared flux density; (b) near-infrared colors, [H/K & [J/K]; (c) mid-infrared/radio flux density; (d) MIR/radio colors, [LW2/LW3], [LW8/LW3] & [radio/LW3].

Fig 9—Cross-section flux density & color profile of the UGC 12915 disk. At each point along the cross-section (see Fig 7) the flux density is integrated in a 6″ radius circular aperture. (a) near-infrared flux density; (b) near-infrared colors, [H/K & [J/K]; (c) mid-infrared/radio flux density; (d) MIR/radio colors, [LW2/LW3], [LW8/LW3] & [radio/LW3].

Fig 10—Cross-section flux density & color profile of the UGC 12914/5 disks plus intergalactic bridge. At each point along the cross-section (see Fig 7) the flux density is integrated in a 6″

radius circular aperture. (a) near-infrared flux density; (b) near-infrared colors, [H/K & [J/K]; (c) mid-infrared/radio flux density; (d) MIR/radio colors, [LW2/LW3], [LW8/LW3] & [radio/LW3].

Fig 11—Mid-infrared spectra of (top panel) UGC 12915 and (bottom panel) UGC 12914. The units are flux density (Jy) vs. wavelength. The PHT-S aperture size is 24″×24″ with 0.1 μm per pixel element. The relative uncertainties in the pixel values are denoted by the 1-σ errorbars. The absolute uncertainty (in the flux density) is estimated to be 30%. A composite mid-IR spectrum (from Lu et al. 1998; generated from a linear combination of spectra from 28 normal galaxies) is denoted with dashed line (redshift corrected to the VV 254 frame of reference). The major Aromatic Feature emission lines are demarked with vertical dashes. The λ-widths of the ISOCAM broad band filters are also indicated.

TABLE 1. Mid & Near-IR Photometry Results for VV254

aperture centering	R″	LW1 (mJy)	LW2 (mJy)	LW8 (mJy)	LW3 (mJy)	J (mJy)	H (mJy)	K (mJy)	J (mag)	H (mag)	K (mag)
UGC 12914	35	47.9	113.5	168.0	167.9	122.0	157.8	130.3	10.30	9.58	9.32
UGC 12915	30	24.5	183.1	225.3	275.5	65.2	91.2	82.0	10.98	10.18	9.83
System center	10	0.8	4.7	7.4	8.2	2.5	2.9	2.4	14.53	13.91	13.64
combined	60	63.7	326.5	437.7	488.2	208.8	273.6	232.5	9.72	8.99	8.69

Notes:

The distance to VV254 is ~61 Mpc (H0 = 75 km/s Mpc^-1), so a radius of 10" corresponds to ~3.0 Kpc.

IRAS Flux Densities: 430, 880, 6300, 13400 mJy at 12, 25, 60 & 100 λm (Soifer et al. 1989)

TABLE 2. VV 254 Global Colors

center	R"	[LW1/LW3]	[LW2/LW3]	[LW8/LW3]	[J/K]	[H/K]
UGC 12914	35	-0.545	-0.170	0.000	-0.028	0.083
UGC 12915	30	-1.051	-0.177	-0.087	-0.100	0.046
"bridge"	10	-1.011	-0.242	-0.045	0.018	0.082
combined	60	-0.884	-0.175	-0.047	-0.047	0.071

Table Notes: color == log10 [flux density (band 1) / flux density (band 2)]

TABLE 3. VV 254 Bridge Dust Emission Spectrum

bandpass	$\log(\nu L_\nu)$ $L_\odot$	$4\pi\nu I_\nu / N_H$ (10^{-31} W/H atom)	I_ν / N_H (MJy/sr/10^{20}Hcm^{-2})
LW1(4.5μm)	<7.8	<0.3	<3.6(-3)
LW2(6.8μm)	8.38	1.18	2.1(-2)
LW8(11.4μm)	8.35	1.10	3.3(-2)
LW3(15.0μm)	8.28	0.93	3.7(-2)

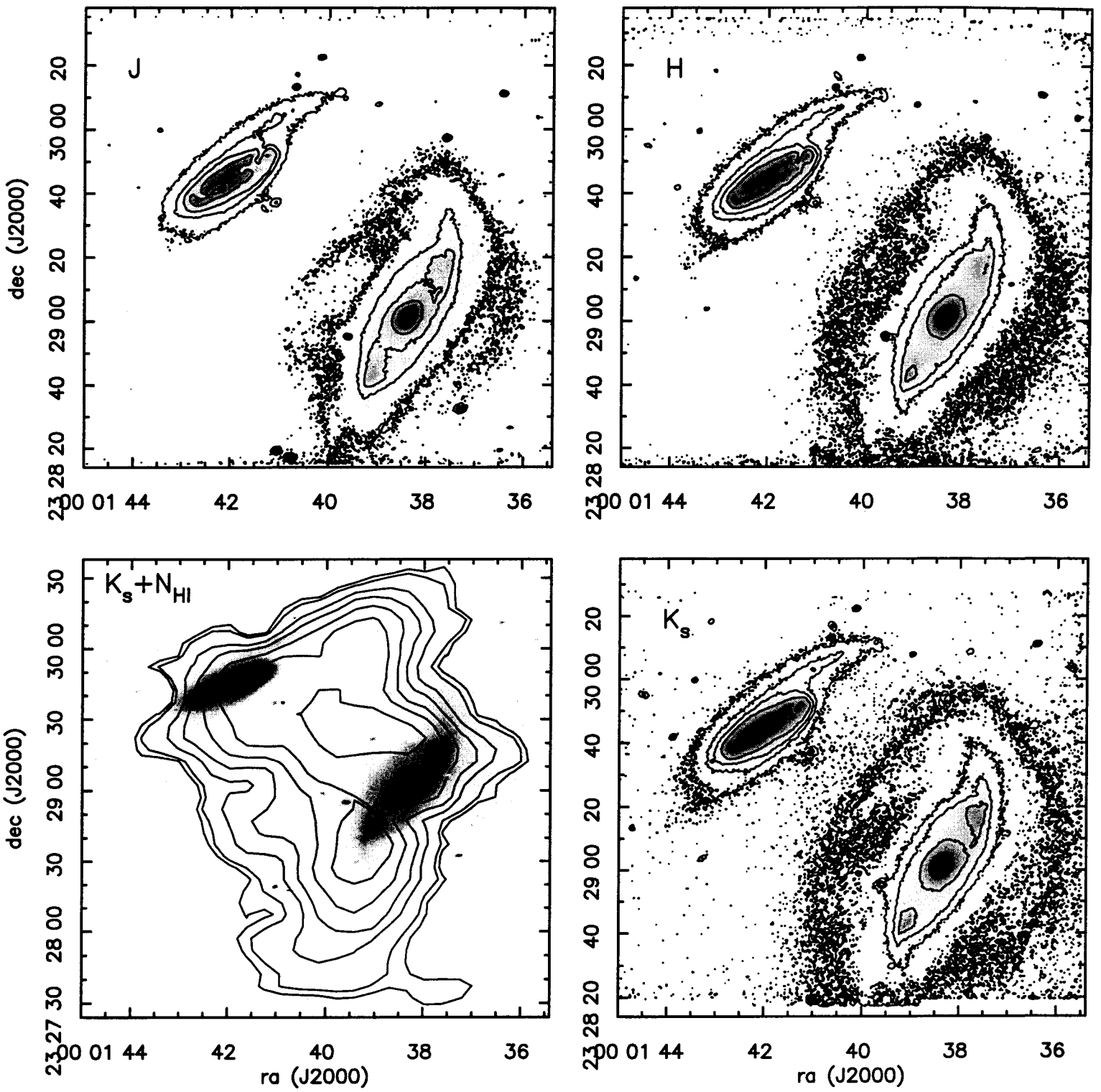
J
H
K_s+N_{HI}
K_s
dec (J2000)
ra (J2000)
23 28 20
30 00 20
29 00 20
28 00 30
27 30
00 01 44
42
40
38
36

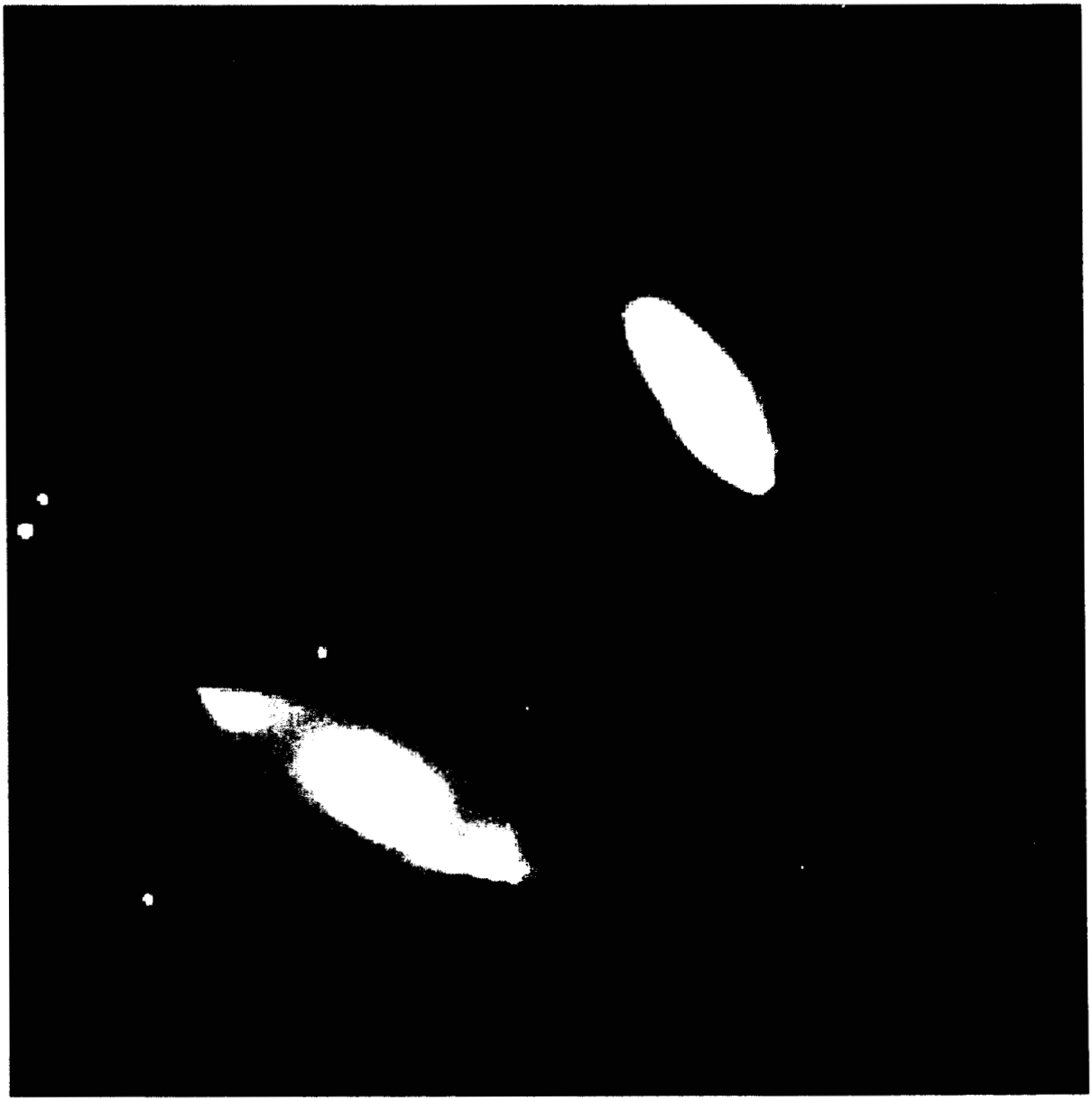

Fig 3b

Jarrett et al

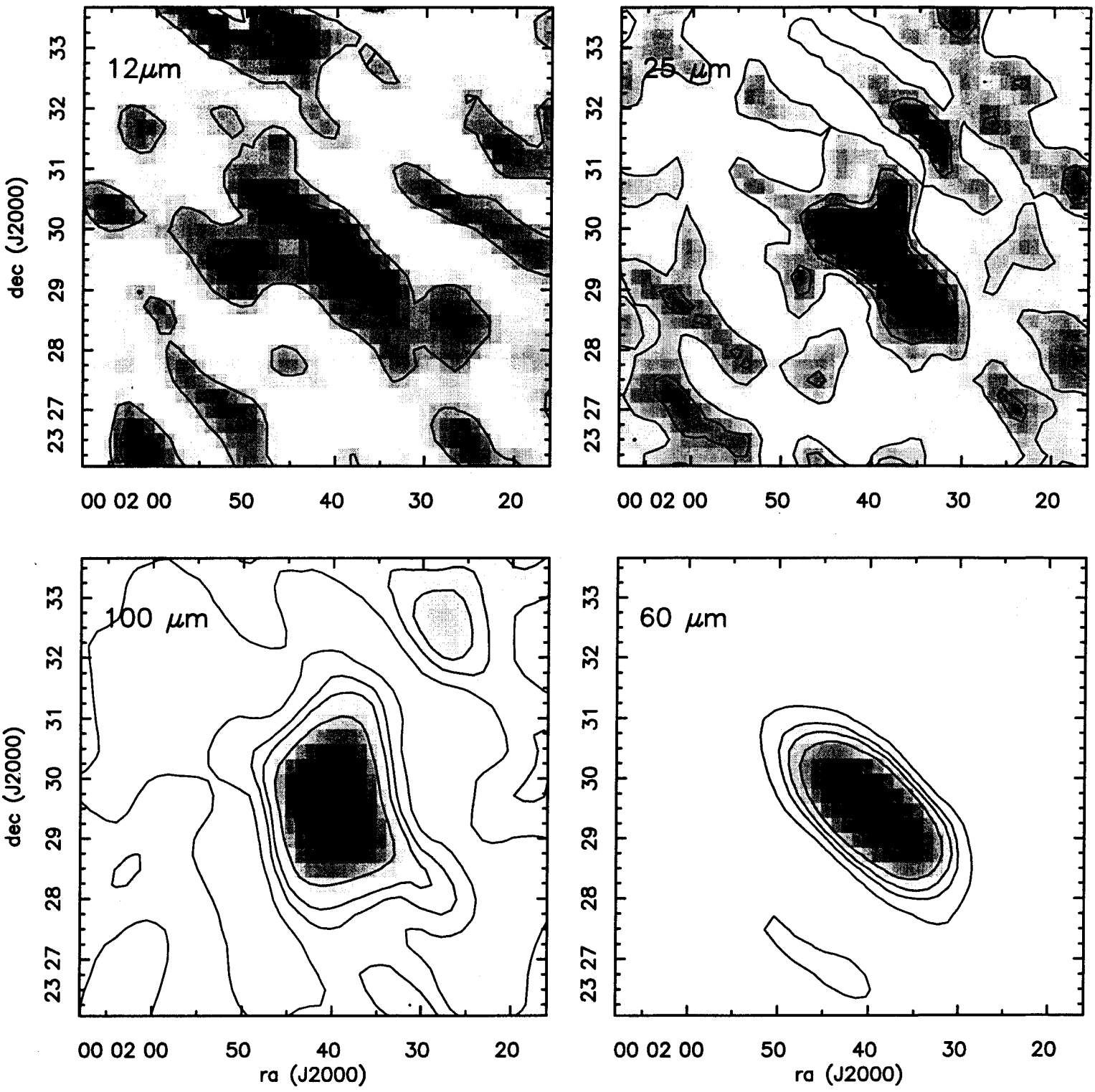
12μm
25 μm
100 μm
60 μm
dec (J2000)
ra (J2000)
23 27
28
29
30
31
32
33
00 02 00
50
40
30
20

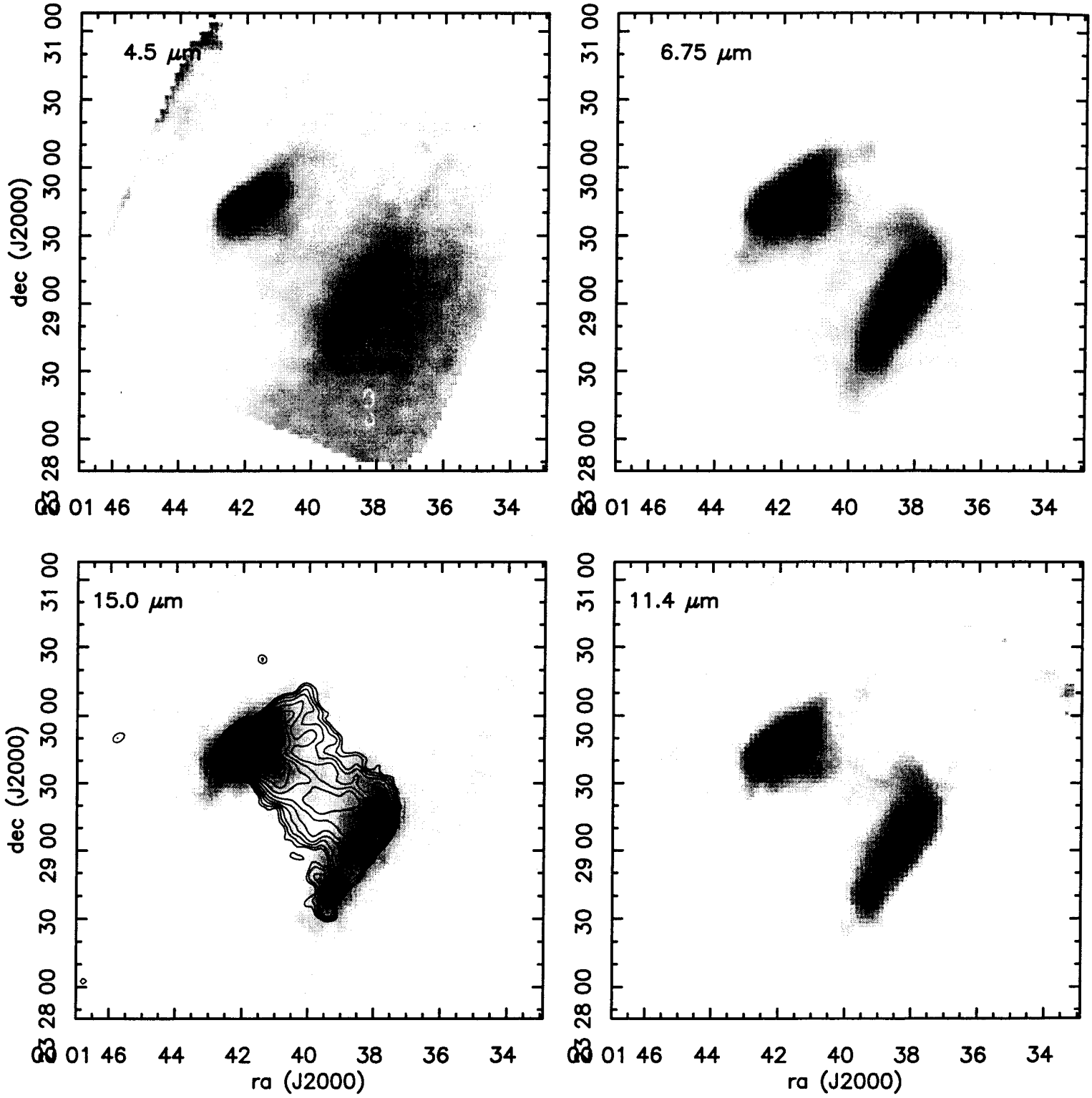
4.5 μm
6.75 μm
15.0 μm
11.4 μm
dec (J2000)
ra (J2000)
23 01 46 44 42 40 38 36 34
28 00 30 29 00 30 30 00 30 31 00

Fig 6a
Jarrett et al.

Fig 6b
Jarrett et al.

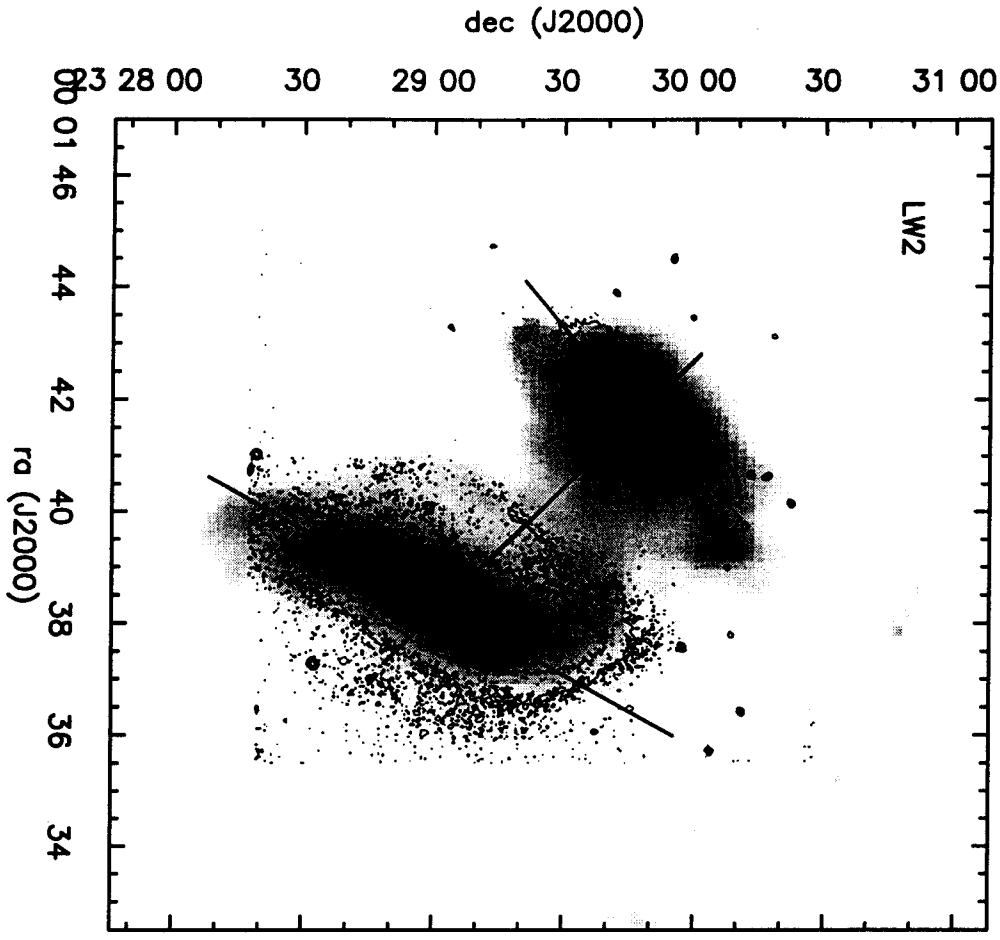
dec (J2000)
23 28 00
30
29 00
30
30 00
30
31 00
00 01 46
44
42
40
38
36
34
ra (J2000)
LW2

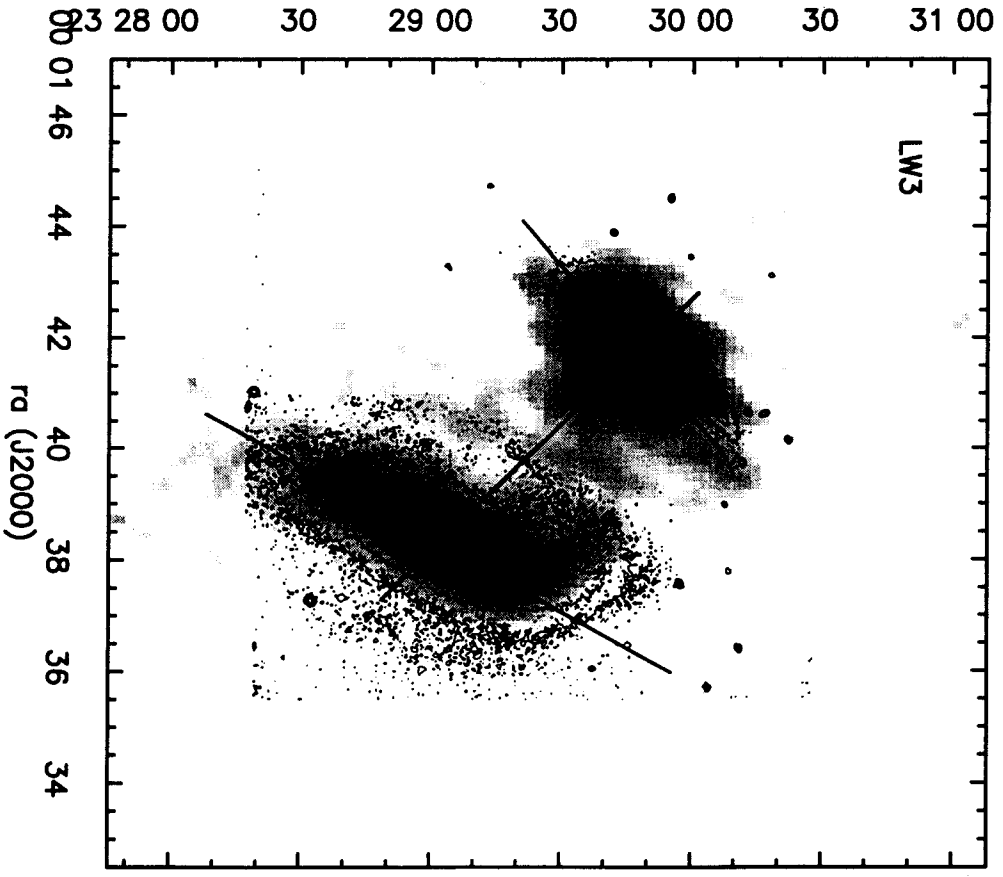
23 28 00
30
29 00
30
30 00
30
31 00
00 01 46
44
42
40
38
36
34
ra (J2000)
LW3

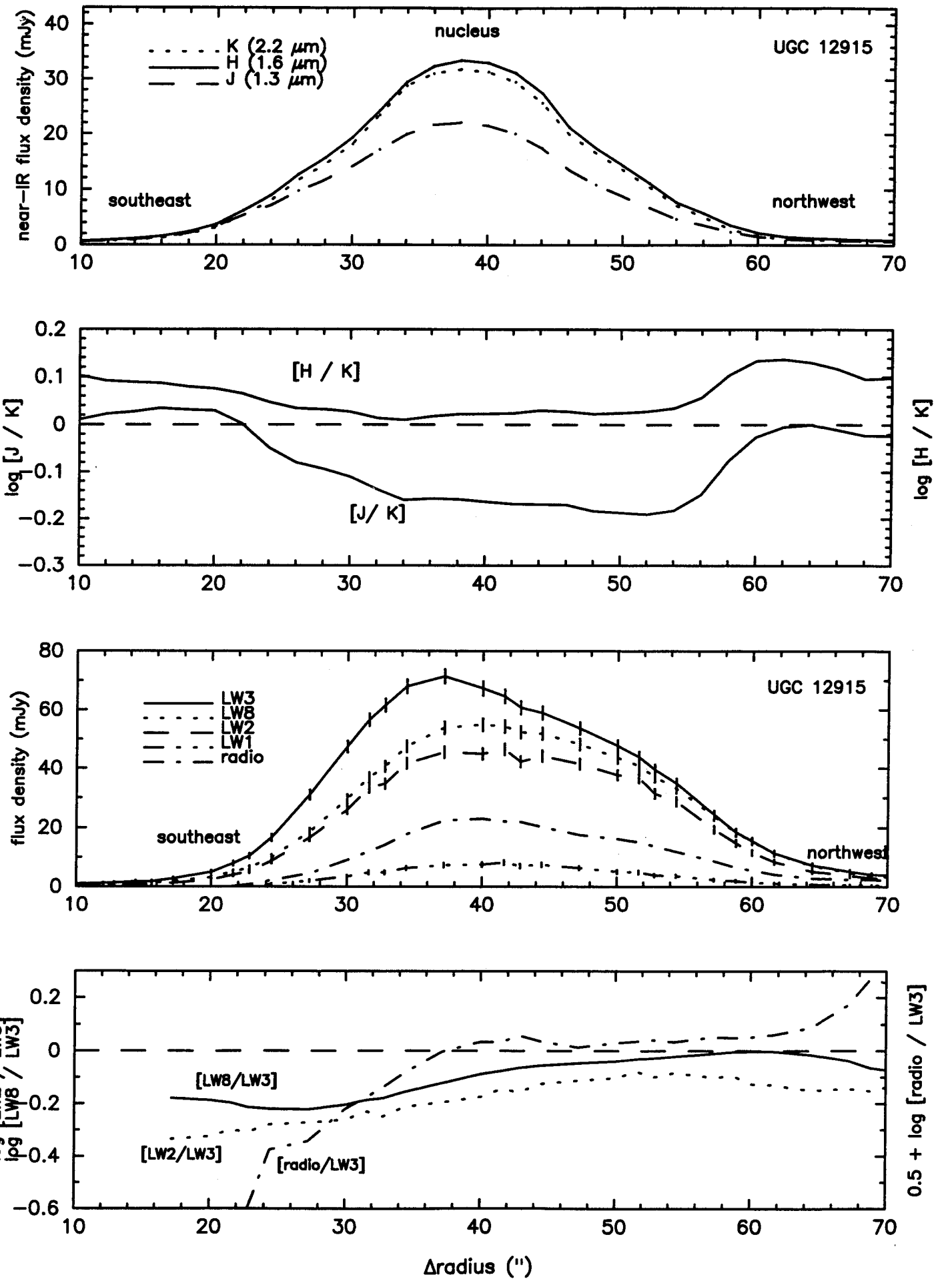
near−IR flux density (mJy)
nucleus
UGC 12915
K (2.2 μm)
H (1.6 μm)
J (1.3 μm)
southeast
northwest
log [J / K]
[H / K]
[J/ K]
log [H / K]
flux density (mJy)
UGC 12915
LW3
LW8
LW2
LW1
radio
southeast
northwest
log [LW2 / LW3]
log [LW8 / LW3]
[LW8/LW3]
[LW2/LW3]
[radio/LW3]
0.5 + log [radio / LW3]
Δradius (")

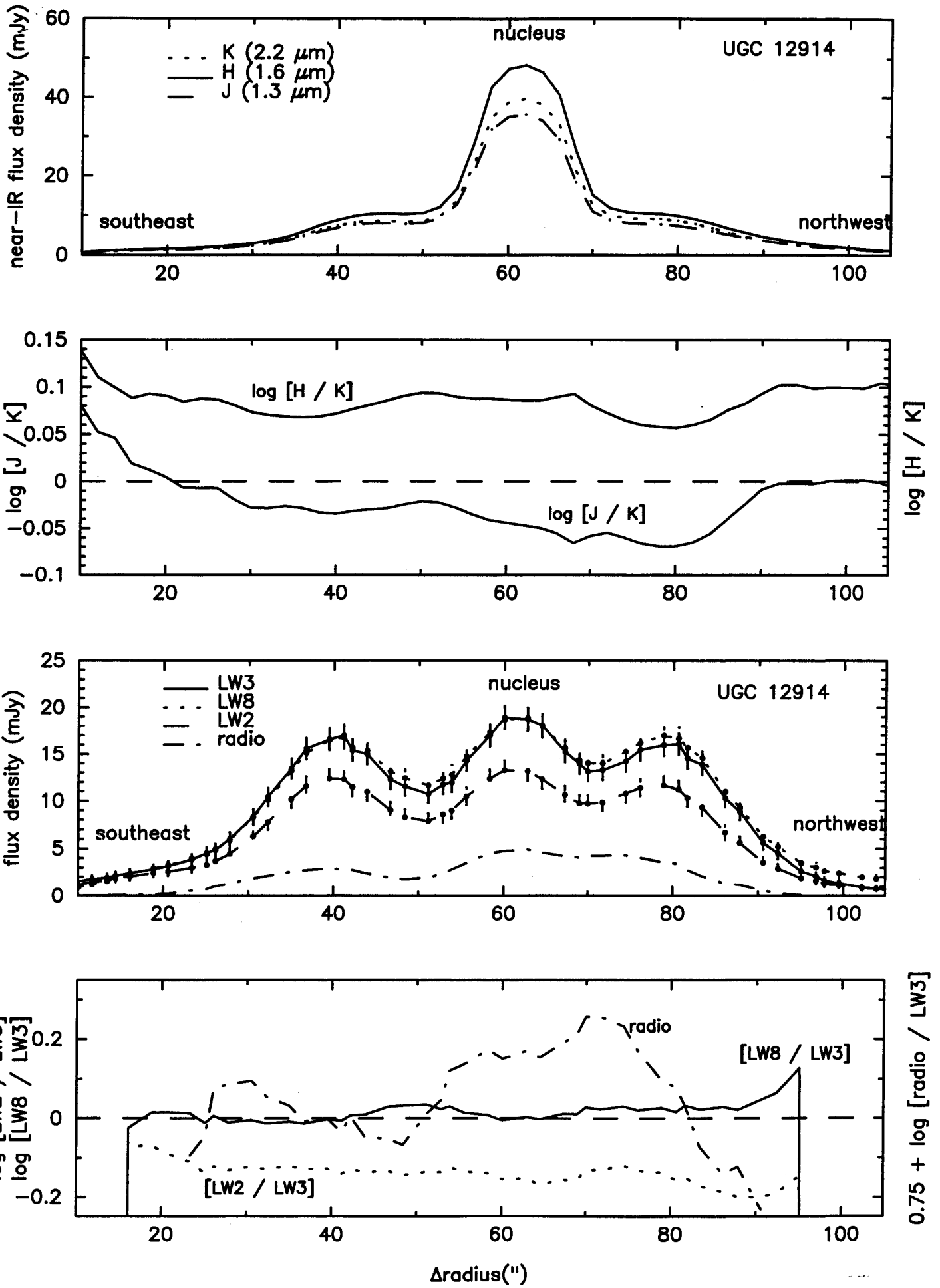
near−IR flux density (mJy)
K (2.2 μm)
H (1.6 μm)
J (1.3 μm)
nucleus
UGC 12914
southeast
northwest
log [J / K]
log [H / K]
log [H / K]
flux density (mJy)
LW3
LW8
LW2
radio
nucleus
UGC 12914
southeast
northwest
log [LW2 / LW3]
log [LW8 / LW3]
radio
[LW8 / LW3]
[LW2 / LW3]
0.75 + log [radio / LW3]
Δradius(")

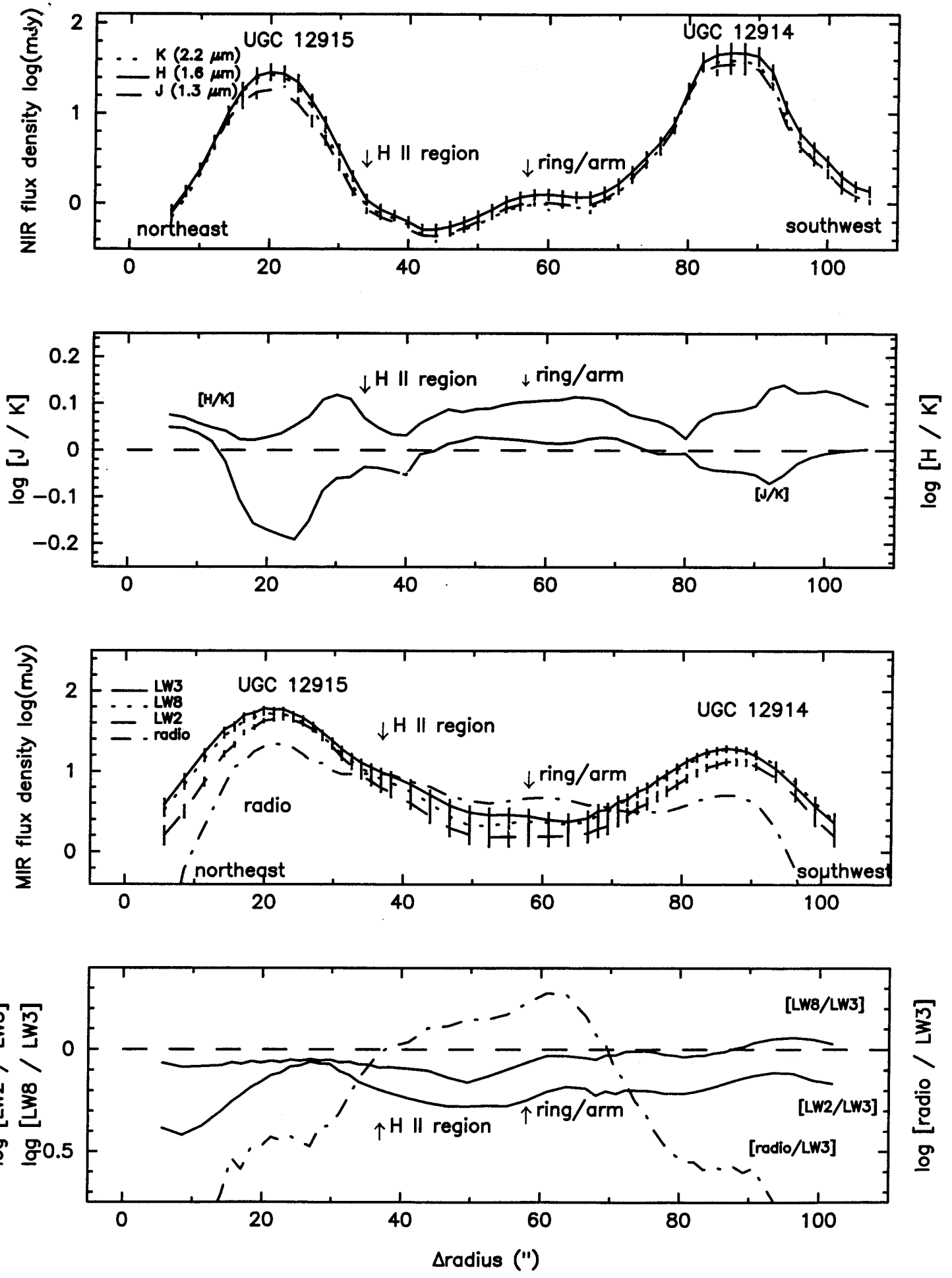
NIR flux density log(mJy)
UGC 12915
UGC 12914
K (2.2 μm)
H (1.6 μm)
J (1.3 μm)
↓H II region
↓ring/arm
northeast
southwest
log [J / K]
log [H / K]
[H/K]
[J/K]
MIR flux density log(mJy)
LW3
LW8
LW2
radio
log [LW2 / LW3]
log [LW8 / LW3]
log [radio / LW3]
[LW8/LW3]
[LW2/LW3]
[radio/LW3]
↑H II region
↑ring/arm
Δradius (")

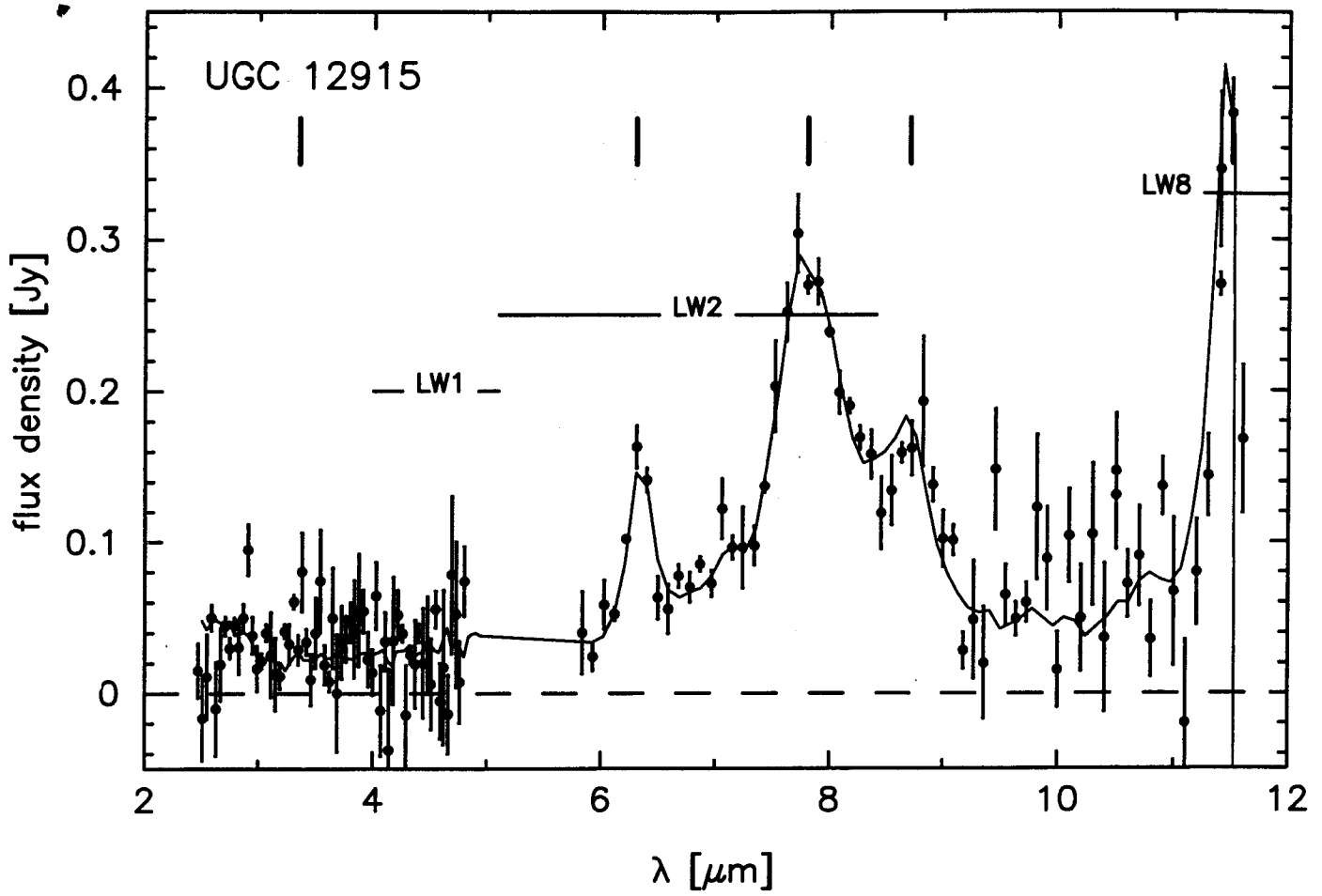
UGC 12915
LW1
LW2
LW8
flux density [Jy]
λ [μm]
0.4
0.3
0.2
0.1
0
2
4
6
8
10
12

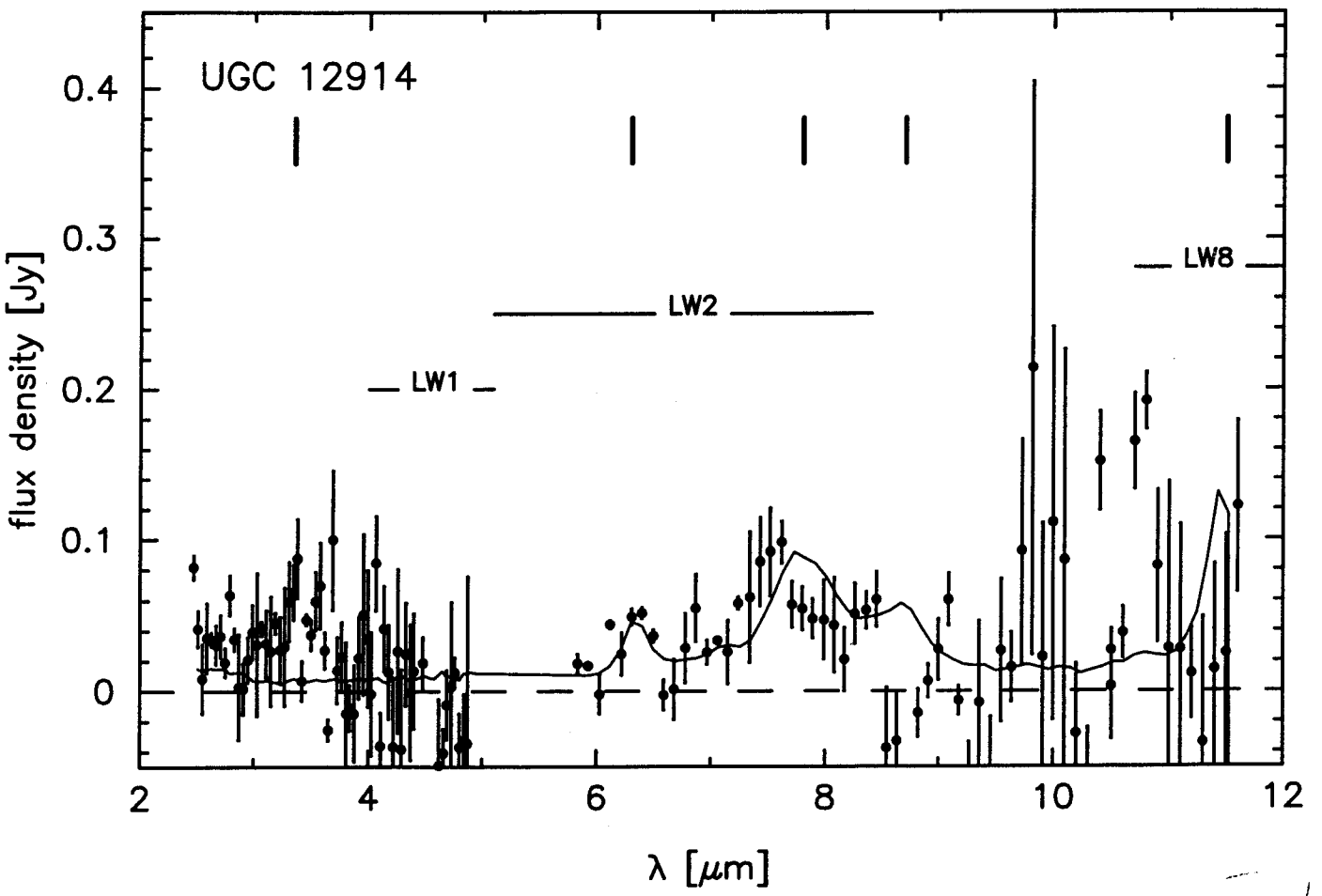
UGC 12914
LW1
LW2
LW8
flux density [Jy]
λ [μm]
0.4
0.3
0.2
0.1
0
2
4
6
8
10
12